## Miniature magnetic rod interfacial stress rheometer for general-purpose microscopes

Yiming Qiao, Chen Fan, Zhengyang Liu, et al.

Citation: Journal of Rheology 65, 1103 (2021); doi: 10.1122/8.0000263

View online: https://doi.org/10.1122/8.0000263

View Table of Contents: https://sor.scitation.org/toc/jor/65/6

Published by the The Society of Rheology

## ARTICLES YOU MAY BE INTERESTED IN

Robust networks of interfacial localized graphene in cocontinuous polymer blends Journal of Rheology **65**, 1139 (2021); https://doi.org/10.1122/8.0000294

Entangled linear polymers in fast shear flows: Comparison of tube-model predictions and experimental data Journal of Rheology **65**, 1111 (2021); https://doi.org/10.1122/8.0000280

Entrance flow of unfoamed and foamed Herschel–Bulkley fluids Journal of Rheology **65**, 1155 (2021); https://doi.org/10.1122/8.0000286

Wall effect on the rheology of short-fiber suspensions under shear Journal of Rheology **65**, 1169 (2021); https://doi.org/10.1122/8.0000292

Stress versus strain controlled shear: Yielding and relaxation of concentrated colloidal suspensions Journal of Rheology **65**, 1219 (2021); https://doi.org/10.1122/8.0000212

Shear-banding fluid(s) under time-dependent shear flows. Part I: Spatiotemporal dynamics Journal of Rheology **65**, 1187 (2021); https://doi.org/10.1122/8.0000303

DISCOVER the RHEOMETER with the...

Sensitivity • Ease-of-use • Versatility

to address the most demanding applications

The **NEW Discovery Hybrid Rheometer** 



# Miniature magnetic rod interfacial stress rheometer for general-purpose microscopes

Yiming Qiao, Chen Fan, Zhengyang Liu, Dani Medina, Nathan C. Keim, and Xiang Cheng, and Xiang Cheng, Viming Qiao, Chen Fan, Xiang Cheng, Dani Medina, Nathan C. Keim, And Xiang Cheng, Dani Medina, Nathan C. Keim, Nathan C.

<sup>1</sup>Department of Chemical Engineering and Materials Science, University of Minnesota, Minneapolis, Minnesota 55455 <sup>2</sup>Department of Physics, California Polytechnic State University, San Luis Obispo, California 93407  $^3$ Department of Physics, Pennsylvania State University, University Park, Pennsylvania 16802

(Received 24 February 2021; final revision received 12 July 2021; published 7 September 2021)

#### **Abstract**

Despite the great demand for the characterization of interfacial rheology in academic and industrial research, the study of interfacial rheology is still scarce compared to its counterpart of bulk rheometry and limited only to specialized laboratories. One of biggest hurdles impeding the broad application of interfacial rheometry is the delicate design and the high cost of interfacial rheometers. Here, we propose a new design of a miniature magnetic rod interfacial stress rheometer (mini-ISR), which uses a pair of small permanent magnets as a magnetic trap and a single magnetic coil for perturbation. The simple design of our ISR substantially reduces its dimension, allowing us to directly couple the rheometer to a conventional commercial optical microscope. Such unprecedented adaptability makes the new ISR highly portable and cost-effective. Moreover, the use of a commercial microscope improves the imaging quality and lowers the difficulty of synchronized imaging of interfacial rheometry. We show the calibration of the mini-ISR and demonstrate its functionality by measuring the interfacial rheology and imaging the microscopic dynamics of particle monolayers at a water-oil interface. Our design can be used by any laboratories that have access to optical microscopes for a wide range of interfacial rheology studies. © 2021 The Society of Rheology. https://doi.org/10.1122/8.0000263

### I. INTRODUCTION

Materials at the fluid-fluid interface exhibit properties different from those in bulk phases [1]. A fluid-fluid interface decorated with surface active materials such as colloidal particles, macromolecules, or surfactants can show complex dynamics and viscoelastic behaviors in response to interfacial deformations [2]. Understanding the interfacial dynamics and mechanical properties of complex fluid-fluid interfaces is of importance in controlling and designing various interface-rich materials like emulsions and foams, which play critical roles in many industrial applications such as drug delivery and oil recovery [3,4]. However, in contrast to bulk rheometery, measurements of interfacial rheology are intrinsically difficult and often subject to large experimental errors. In particular, the sensitivity of interfacial rheometers is strongly affected by the unavoidable coupling between interfacial and bulk flows [4,5]. For a rheological probe placed at an interface, the Boussinesq number Bq is usually used to characterize the strength of this coupling, which is defined as the ratio of the contribution to the drag on the probe from the interface to that from the subphase,

$$Bq = \frac{\eta_s}{\eta_b \cdot a}. (1)$$

Here,  $\eta_s$  is the interfacial viscosity,  $\eta_b$  is the bulk viscosity, and a is the characteristic length scale depending on the specific rheometer geometry [4]. For a viscoelastic interface, the interfacial viscosity  $\eta_s$  and the corresponding Boussinesq number Bq can be complex. To achieve a high sensitivity for interfacial rheology, a large Bq is necessary. When  $|Bq| \gg 1$ , the drag exerted on the rheological probe predominantly arises from the interface, while the contribution from the bulk is negligible.

Much effort has been put into rheometer designs for improving the sensitivity of interfacial rheology measurements. Different interfacial rheometers including canal devices [6], knife-edge devices [7], rotating disks and rings [8,9], and channel flow devices [10] have been invented. With small characteristic lengths a, magnetic rod interfacial stress rheometers (ISRs) stand out among these designs due to their potential for high sensitivity and a well-defined shear flow field [5,11]. First realized by Shahin [12] and further developed by Brooks et al. [13], a typical ISR uses a slender magnetic needle as the probe between two pairs of Helmholtz coils, where one pair creates a constant magnetic field for controlling the needle orientation and the other provides a timevarying magnetic field gradient to oscillate the needle. ISRs have been employed for various interfacial rheological measurements on colloidal particles, proteins and lipopolymers [5,11,13–17]. In addition, there has been great progress in improving the sensitivity of ISRs by using magnetic microwires with small diameters [3,4] and developing a theoretical framework based on the Navier-Stokes equations [4,18], where the detailed velocity profile of sheared samples provides crucial information guiding the given rheological test [19].

Nevertheless, direct imaging of the flow at an interface by coupling ISR with optical microscopes is still difficult.

a)Electronic mail: keim@psu.edu

b) Author to whom correspondence should be addressed; electronic mail: xcheng@umn.edu

The magnetic coils in a conventional ISR must be separated by a distance equal to their radii, which typically requires a custom microscope to fit between the coils. Recently, Tajuelo et al. showed that a pair of stationary permanent magnets could form a magnetic trap for the needle. By installing the magnets on a large precision linear translation stage, they manipulated the needle and measured interfacial viscosities as low as  $10^{-9} \,\mathrm{N} \cdot \mathrm{s/m}$  [11]. However, the appropriate translation stage is expensive, and it is difficult to precisely synchronize the rheometer with the camera. Here, we propose a new design for a miniature interfacial stress rheometer (mini-ISR) using a pair of stationary permanent magnets for a magnetic trap and a single magnetic coil to control the needle oscillation. By replacing bulky Helmholtz coils in existing ISRs with small stationary permanent magnets, we have achieved the most compact ISR design to date. The small dimension allows us to directly couple the rheometer to a conventional commercial microscope without any modification of the microscope. The new design gains significant advantages thanks to this adaptability. First, modern commercial microscope systems are highly developed, with high performance and user-friendly interfaces, which are hard to match with homemade imaging systems used by existing interfacial rheometers. Second, without a custom imaging system and with the compact design, our new ISR becomes highly portable and can be easily moved and shared by researchers in different laboratories. Last, since standard optical microscopes are accessible to most research laboratories, by avoiding the construction of custom imaging systems, our design substantially lowers the construction cost of ISRs, a crucial factor hindering the broad application of interfacial rheometry. As such, our design of mini-ISR provides a sensitive, highly portable, and adaptable device for synchronous measurements of the microscopic dynamics and the macroscopic rheology and velocity profile of complex fluid interfaces, which facilitates the application of interfacial rheometry in academic and industrial research.

Below, we shall first present the simple design of our ISR. We will then discuss the detailed calibration process and demonstrate the function of the mini-ISR by measuring the interfacial rheology and imaging the microscopic dynamics of particle monolayers at a water-oil interface.

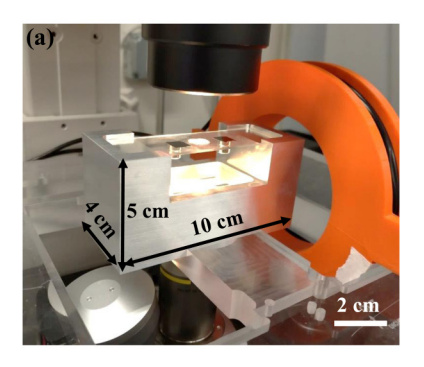
## II. MINI-ISR

## A. Design

The picture and the schematic of our mini-ISR setup are shown in Figs. 1(a) and 1(b). A trough with a dimension of  $10 \times 4 \,\mathrm{cm}^2$  and a height of 5 cm is placed on the stage of an inverted microscope (Nikon, Ti-E). An open-end shearing channel with a length of 2 cm, a width of 6 mm, and a height of 7 mm is constructed from glass slides in the center of the trough [Fig. 1(c)]. A window of  $3 \times 3 \text{ mm}^2$  is created for visualization at the bottom of the trough and sealed by a microscope coverslip. On the top of the trough, we attach a pair of permanent magnets (neodymium, McMaster-Carr) onto a piece of glass slide and fix the distance between the magnets at 3.0 cm. A magnetic needle with a radius of  $79.2 \,\mu m$  and a length of 2.45 cm is used as the rheological probe in our study. The large aspect ratio of the needle results in a large Boussinesq number and, therefore, a high sensitivity [3,13]. The permanent magnets are fixed 3.3 cm above the needle, and the field of the magnets aligns the needle parallel to the shearing channel. In addition, we use a single magnetic coil with a power amplifier (PA-151, Labworks Inc.) to generate the perturbative field, which drives the oscillation of the needle at a water-decane interface (preparation details in Subsection 2 of the Appendix). The magnitude and frequency of the applied strain can be readily adjusted by changing the oscillating current of the magnetic coil. We image the interface through a 10× lens (Nikon, NA 0.30, WD 17.0 mm) with a synchronized high-resolution CMOS camera (Basler acA2040-90um USB 3.0) (synchronization details in Subsection 1 of the Appendix).

## **B.** Calibration

To calibrate the ISR, we analyze the movement of the needle. Figure 2(a) shows a typical image of the needle at a clean fluid-fluid interface. The shape of the needle can be identified with subpixel resolution using the algorithm in [17,20]. We track the motion of random asperities on the edges of the needle [Fig. 2(b)], which gives the trajectory of the needle in Fig. 2(c). In previous studies, the probe position was always measured by tracking the end of the needle



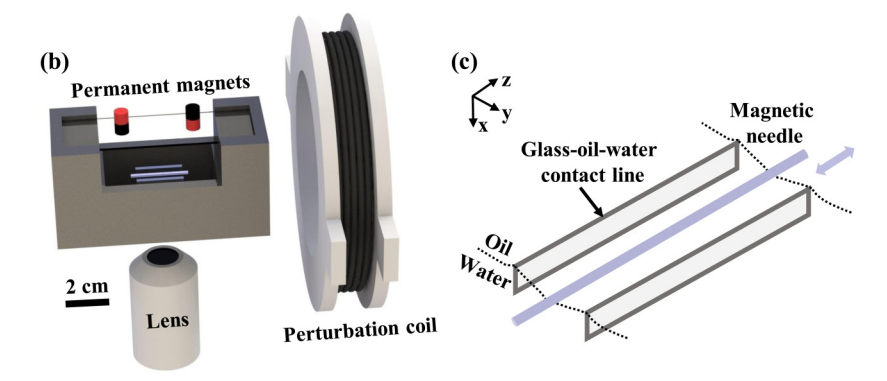


FIG. 1. Design of mini-ISR. (a) A picture of the mini-ISR mounted on an inverted microscope. (b) A schematic of the mini-ISR. (c) A schematic of the open-end shear channel formed by two glass coverslips. The magnetic needle is embedded in the water-oil interface. The arrow indicates its shearing motion driven by the perturbation coil. Dashed lines illustrate the position of the meniscus of the interface.

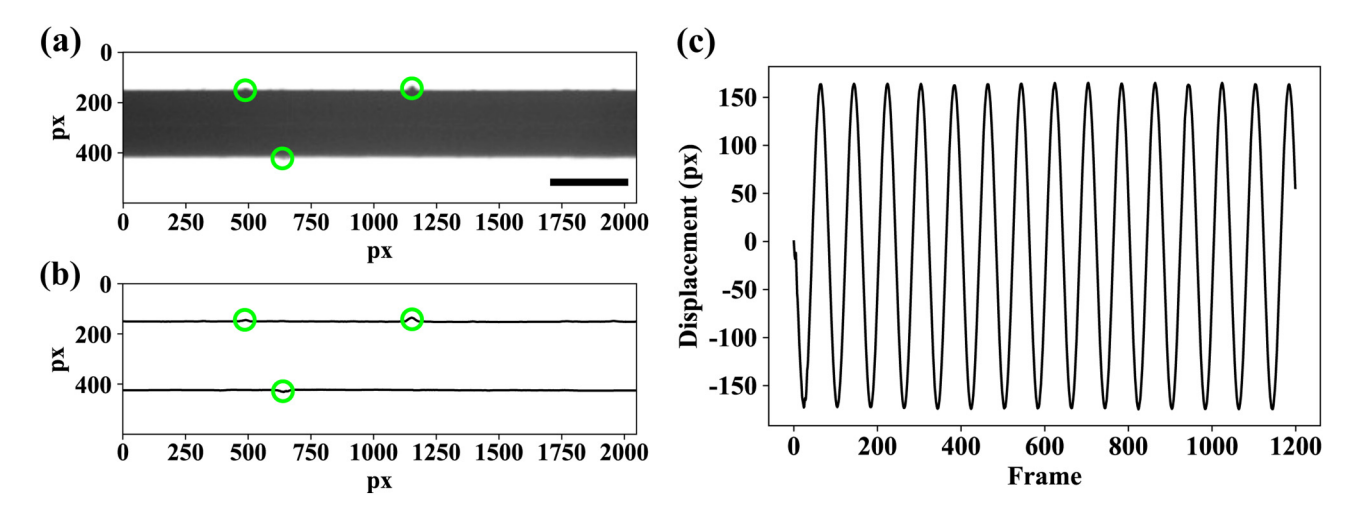


FIG. 2. Tracking the needle motion. (a) A typical image of the needle. Scale bar =  $200 \,\mu\text{m}$ . (b) The needle edges identified by a custom algorithm. The circles highlight random bumps on the needle. The displacements of bumps under a sinusoidal shear are traced and the needle trajectory can be obtained, as shown in (c). The frame rate is 80 frames/cycle and the shearing frequency is 0.2 Hz.

[3,4,11,13–15,19,21]. With a single microscope, such a practice cannot image interfacial materials in the middle of the probe without potential end effects. In contrast, by tracking small random asperities on the surface of the needle, we *simultaneously* image the probe position and the microscopic dynamics of the monolayer avoiding end effects.

The equation of motion for the needle at a clean fluidfluid interface can be modeled as

$$m\ddot{z} = AI_{\text{drive}} - kz - d\dot{z},\tag{2}$$

where m is the inertial mass of the needle, z is the displacement,  $\dot{z}$  and  $\ddot{z}$  are the velocity and acceleration of the needle,  $I_{\rm drive}$  is the perturbation current,  $AI_{\rm drive}$  is the resulting force, k is an effective spring constant, and d is the drag coefficient. The right-hand side of Eq. (2) details the total force on the needle, which is composed of the magnetic force generated by the magnetic coil, the restoring force provided by the permanent magnets, and the drag force from bulk phases. Figure 3 shows the analysis of forces on the needle from a front view, as well as the geometry from the top view. Note

that the restoring force -kz in Eq. (2) is provided by the permanent magnets rather than the Helmholtz coils in a traditional ISR. To demonstrate that this restoring force is harmonic, we plot the needle displacement amplitude versus the perturbation current amplitude at a clean water-oil interface over the full range of needle displacement z explored in our study [Fig. 3(b)]. The linear relation between z and  $I_{\rm drive}$  verifies the harmonic nature of the magnetic trap.

Equation (2) shows that the needle can be considered as a damped oscillator. As a result, we can quantify the behavior of the mini-ISR by the phase angle ( $\delta$ ) and the amplitude ratio (AR) between the needle displacement and the driving force [22],

$$\delta(\omega) = \arctan\left[-\frac{\omega d}{k - m\omega^2}\right],\tag{3}$$

$$AR(\omega) = \frac{z}{AI_{\text{drive}}} = \frac{1}{\sqrt{(k - m\omega^2)^2 + (\omega d)^2}},$$
 (4)

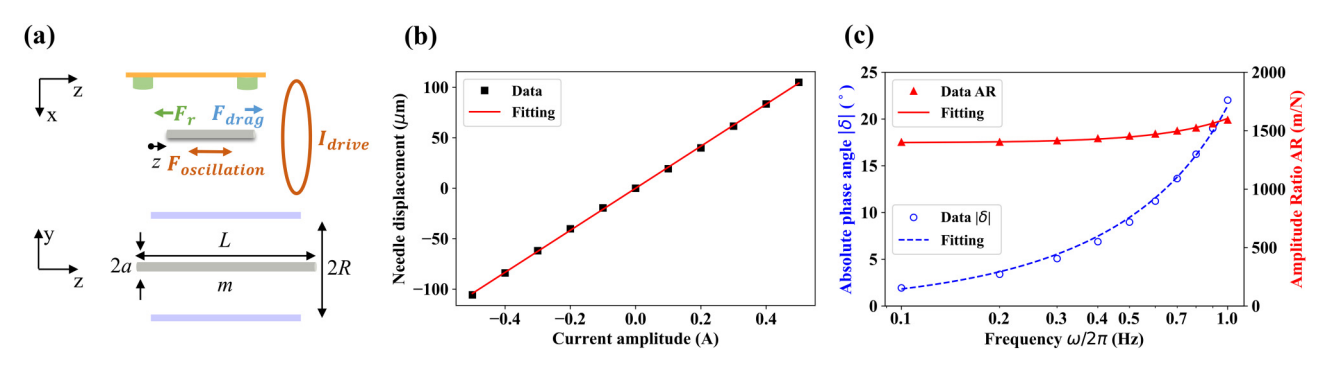


FIG. 3. Mini-ISR calibration at a clean water-decane interface. (a) A schematic showing the forces acting on the needle (upper half), with the dimensions of ISR rheometry indicated (lower half) L=2.45 cm, R=3 mm,  $a=79.2\,\mu\text{m}$ , and m=3.44 mg. The restoring force,  $F_{\text{r}}$ , is provided by the permanent magnets. The drag force,  $F_{\text{drag}}$ , is exerted on the needle by bulk phases. The oscillation force,  $F_{\text{oscillation}}=AI_{\text{drive}}$ , is provided by the perturbation current. z is the displacement of the needle from its equilibrium position. (b) Needle displacement amplitude versus perturbation current amplitude. The black squares are data points and the red line is the linear fitting. (c) Calibration curves, with triangles and circles showing the data points for the amplitude ratio, AR, and the phase angle,  $\delta$ , respectively. The solid lines are fitting curves based on Eqs. (3) and (4), respectively.

where  $\omega$  is the oscillation frequency of the needle. Figure 3(c) shows the calibration of the mini-ISR at the water-decane interface, where the circles and triangles are data points for the phase angle ( $\delta$ ) and the amplitude ratio (AR), and the lines are the fitting of Eqs. (3) and (4). Based on the fitting, the constant  $A = 8.84 \times 10^{-8}$  N/A, the drag coefficient  $d = 3.62 \times 10^{-5}$  N·s/m, and the effective spring constant  $k = 7.16 \times 10^{-4}$  N/m. k can be adjusted by changing the distance between the magnets and the needle or using magnets with different dipole moments. The quantitative agreement between the data points and the fitting lines demonstrates that our mini-ISR is effective for interfacial rheological measurements.

Note that the above analysis is without a particle monolayer at the interface, so it characterizes the intrinsic system response. The measured response when the monolayer is present includes the contribution of the system. In order to obtain the monolayer response, the simplest way is to assume the two contributions are additive [4,13], from which the dynamic surface modulus can be calculated as

$$G_{S}^{*} = \frac{(R-a)}{2L} \frac{AI_{\text{drive}}}{z_{\text{monolayer}}} e^{-i\delta_{\text{monolayer}}} - \frac{(R-a)}{2L} \frac{AI_{\text{drive}}}{z_{\text{system}}} e^{-i\delta_{\text{system}}},$$
(5)

where  $G_S^*$  represents the complex modulus of the interfacial particle monolayer,  $z_{\text{monolayer}}$  and  $\delta_{\text{monolayer}}$  are the needle displacement amplitude and the phase angle when the monolayer is present,  $z_{\text{system}}$  and  $\delta_{\text{system}}$  are obtained at the same  $\omega$  and  $AI_{\text{drive}}$  at the clean fluid-fluid interface, a is the needle radius, R is the channel half-width, and L is the length of the needle, as shown in Fig. 3(a).

## C. Working range

We estimate the working range of our mini-ISR. From Eq. (5), a larger shear modulus corresponds to a smaller displacement. Thus, we can estimate the upper limit from the smallest detectable displacement of our system and the largest possible current amplitude,

$$G_{\text{max}}^* = \frac{(R - a)AI_{\text{drive}}}{2L}$$

$$= \frac{(0.004 - 7.62 \times 10^{-5})\text{m}}{2 \times 0.034 \,\text{m}} \frac{8.84 \times 10^{-8} \times 2.0 \,\text{N}}{1 \,\text{px} \times 0.65 \times 10^{-6} \,\text{m/px}}$$

$$= 1.57 \times 10^{-2} \,\text{N/m}. \tag{6}$$

Here, one pixel is used as a safe estimate of the smallest displacement we can extract from experiments. The random fluctuations of the needle position with the presence of interfacial materials are less than 0.2 pixels. Without changing the imaging system, the upper limit on  $G^*$  could be raised by using a higher-current signal amplifier or a coil with more turns.

The lower limit for our ISR is estimated based on two factors. First, the Boussinesq number Bq should be large enough so that accurate results can be obtained with the

linear subtraction method we use here. Thus, we estimate the lower bound by

$$G_{\min}^* = Bq_{\min} \times 2\pi f a \eta$$
  
= 100 \times 2\pi \times 0.1 \times 7.62 \times 10^{-5} \times 0.001 \text{ N/m}  
= 4.79 \times 10^{-6} \text{ N/m}, (7)

where  $\eta$  is the viscosity of bulk phases and  $Bq_{\min}$  is chosen to be 100 according to Ref. [4]. This lower limit on  $G^*$  could be decreased by using a thinner needle. However,  $Bq \lesssim 100$  can be made acceptable through more sophisticated numerical modeling of hydrodynamic stresses and the interfacial velocity profile [3,18,19], beyond the linear subtraction technique used here—potentially allowing meaningful interfacial rheology to be extracted from measurements of arbitrarily small interfacial shear stresses.

Second, at low frequencies, the system resolution—and the ability to measure small interfacial shear stresses reliably—is limited by the stiffness of the magnetic trap k [4]. Measuring small surface moduli involves observing the reduction in the amplitude ratio [AR, as defined in Eq. (4)] when the interfacial material is present, as compared to the AR during calibration on the clean fluid-fluid interface [3,4,11]. If we consider a discernible 5% reduction in the AR, then the minimum surface modulus in our realization should be around  $k/20 = 3.58 \times 10^{-5}$  N/m. Thus, the lower limit on  $G^*$  of our device is predominantly determined by the trapping stiffness k.

To improve this limit, the distance between the permanent magnets and the needle can be increased, or weaker magnets can be used, decreasing k and amplifying the effect of small interfacial shear stresses on the needle's motion. One might imagine that the extreme case  $k \to 0$  could make the rheometer arbitrarily sensitive at low frequency. This possibility has been noted previously as an advantage of the mobile trap ISR, in which there is no stationary trap at all [11]. In practice, however, whether the trap is stationary or mobile, its stiffness must remain large enough to counter the perturbations from capillary interactions, convection, stray magnetic fields, and mechanical disturbances that would otherwise cause the needle to drift away from its desired operating position and possibly exit the trap. In effect, these perturbations are the ultimate limits on sensitivity. Quantifying and minimizing them represents an opportunity for further progress.

# III. INTERFACIAL RHEOLOGY AND STRUCTURE OF PARTICLE MONOLAYERS

To demonstrate the functionality of our mini-ISR, we examine the rheological behaviors of a monolayer of  $4.1 \,\mu\mathrm{m}$  diameter sulfate-modified polystyrene (PS) particles at a water-decane interface with different surface coverages. Details on the monolayer preparation and area fraction determination can be found in Subsections 2 and 3 of the Appendix. Figures 4(a) and 4(b) show a strain sweep at a shearing frequency of 0.5 Hz. The strain amplitude z/(R-a), defined as the needle displacement amplitude divided by the sample dimension between the needle and the wall, is controlled in the range between 0.08% and 1%. The

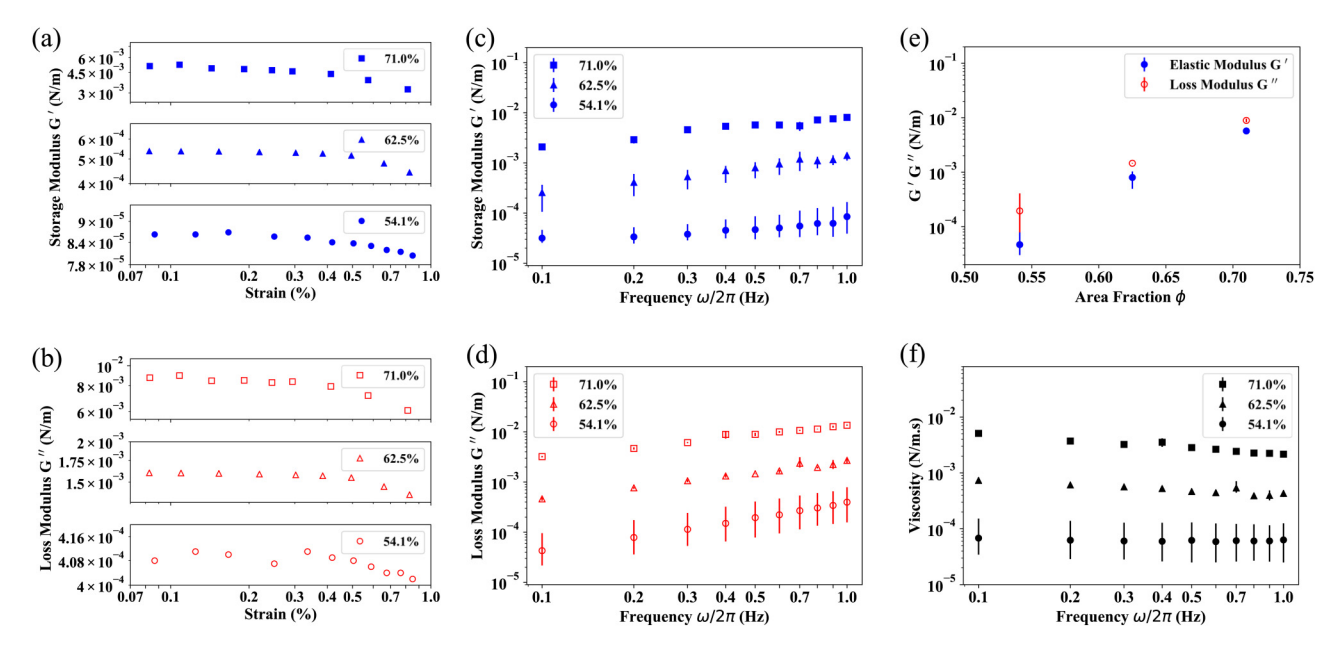


**FIG. 4.** Strain sweeping and frequency sweeping of the rheology of PS particle monolayers with different surface coverages at the water-decane interface. (a) and (b) Storage moduli G' and loss moduli G'' from strain sweeping for strains between 0.08% and 1%, conducted at a shearing frequency of 0.5 Hz. (c) and (d) G' and G'' taken from frequency sweeping for shearing frequencies between 0.1 and 1.0 Hz, conducted at strains less than 0.1%. (e) G' and G'' at the shearing frequency of 0.5 Hz as a function of area fractions. (f) The interfacial viscosity of particle monolayers from the frequency sweeping. The error bars in (c)–(f) indicate the ranges of quantities obtained from multiple independent measurements.

linear viscoelastic region is within 0.1%, which is consistent with previous reports [21,23,24].

Figures 4(c) and 4(d) present frequency-sweep results with shearing frequencies ranging between 0.1 and 1.0 Hz and shear strains in the linear viscoelastic regime. Across different area fractions, we observe three decades of change in the storage moduli and loss moduli, consistent with previous reports [15,21,23,24]. At a given shearing frequency, both storage moduli and loss moduli increase with the area fraction, as shown in Fig. 4(e). Additionally, high-area-fraction monolayers exhibit weak shear thinning, as shown in Fig. 4(f). The trend is also consistent with previous studies [15,23,24].

It is worth noting that for all the measurements in the strain sweep and frequency sweep, the Boussinesq number Bq is always larger than  $10^4$ , which means the stress exerted on the

magnetic needle arises predominantly from the interface. In addition, the Reynolds number  $Re = \rho a^2 \omega / \eta$  is lower than 0.01 at all shearing frequencies. Such a large Bq and a low Re ensure a linear deformation profile at the interface and justify the calculation based on the simple linear subtraction as indicated by Eq. (5) [4,19]. Recently, Fitzgibbon  $et\ al.$  also defined the characteristic length scale for the ISR interfacial flow,

$$\ell_{\omega}^{s} = \sqrt{\ell_{\omega} \frac{\eta_{s}}{\eta_{b}}} = \sqrt{\left(\frac{\nu}{\omega}\right)^{1/2} \frac{\eta_{s}}{\eta_{b}}},\tag{8}$$

where  $\ell_{\omega}$  is the viscous length scale in the bulk fluid,  $\nu$  is the kinematic viscosity of the bulk phase,  $\omega$  is the oscillation frequency,  $\eta_s$  is the interfacial viscosity, and  $\eta_b$  is the viscosity

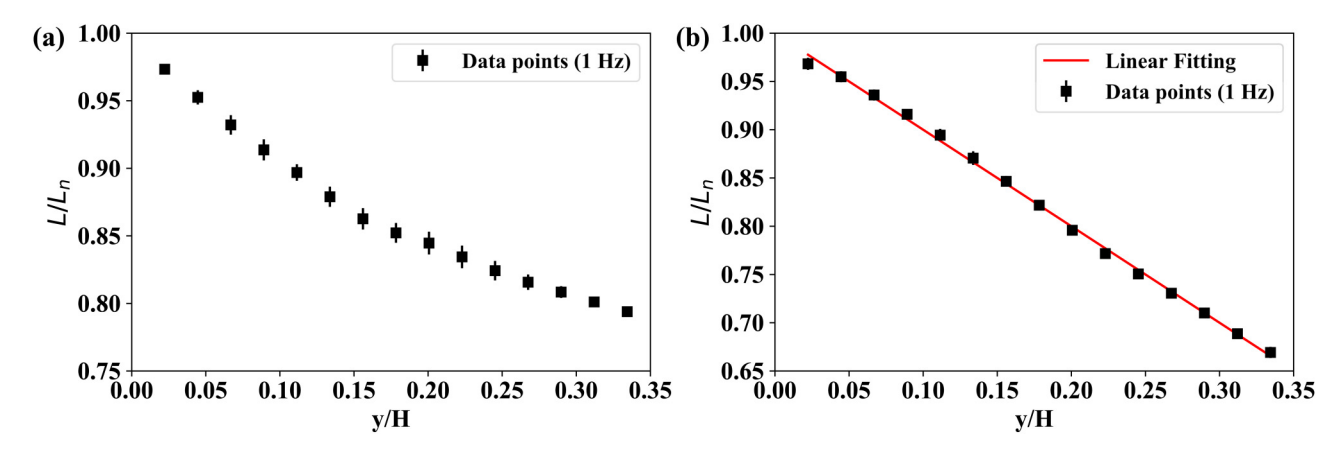


**FIG. 5.** Velocity profiles at area fractions of (a) 45.6% and (b) 54.1% obtained with particle image velocimetry (PIV) [27]. Particle displacements (*L*) are measured over a quarter of one shearing cycle and normalized by the needle displacement ( $L_n$ ). The distance *y* is normalized by the distance between the needle and the wall *H*. The needle edge is at y = 0. The PIV window is a 166.4  $\mu$ m square, translated in steps of 83.2  $\mu$ m, and the error bars represent the standard deviations among all windows at the same *y*.

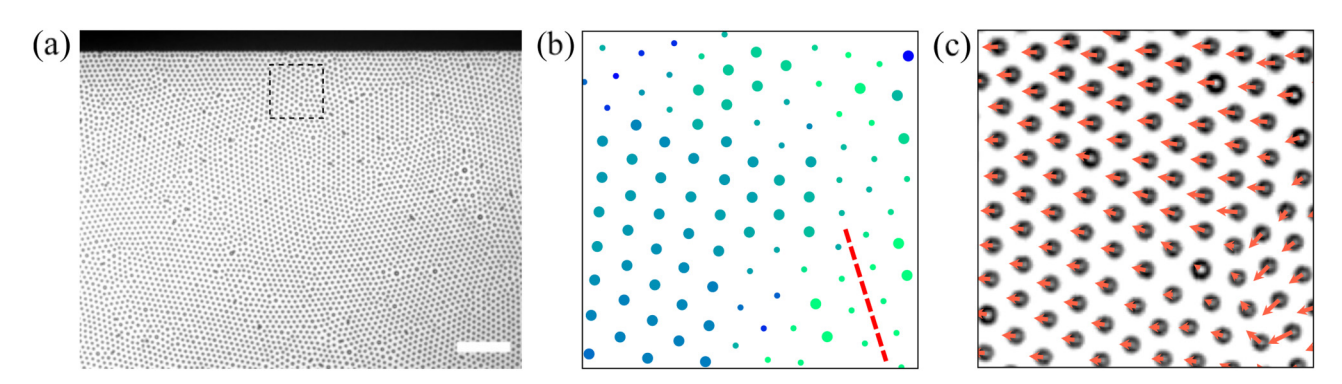


**FIG. 6.** Particle tracking. (a) A snapshot showing the particle monolayer and the needle (the upper black region). Scale bar =  $100\,\mu\text{m}$ . Area fraction = 30.3%. (b) The bond-order parameter of particles in the selected square region in (a). Dot sizes show the relative local bond-order parameter (larger dots represent  $|\psi_6| > 0.9$ ). The dashed line shows the position where the nonaffine particle rearrangements occur. (c) Particle displacements during 0.15 s displaying the rearrangement event. The lengths of the vectors are twice the real particle displacements for visualization purposes.

of bulk fluid [18].  $\ell_{\omega}^{s}$  quantifies the distance over which the momentum decays at the fluid-fluid interface. When  $\ell_{\omega}^{s}$  is larger than the half-channel width R, the interfacial velocity profile will be linear. If  $\ell_{\omega}^{s}$  is smaller than R, a nonlinear velocity profile at the interface will be expected [18,25,26]. For our measurements, the minimum  $\ell_{\omega}^{s}$  can be obtained by using the lowest area fraction (54.1%) and the highest shearing frequency (1 Hz).  $\ell_{\omega}^{s} \gtrsim 16$  mm, five times larger than the half-channel width R = 3 mm. The calculation again justifies the linear subtraction in Eq. (5) implemented in our study.

We also directly measure the velocity profiles of the particle monolayers. Consistent with the above estimate, the velocity profile of the particle monolayer at 54.1% is linear, whereas at an even lower area fraction of 45.6%, the profile shows an obvious deviation from the linear profile (Fig. 5), supporting our decision to exclude those rheology measurements. We note that the position of our microscope within the shearing channel means that velocity profiles can be captured routinely during rheological tests. This allows the validity of the linear subtraction method to be checked empirically [19], and augments the use of theoretical frameworks and numerical results.

The combination of the mini-ISR with the inverted microscope allows us to measure the interfacial rheology and image the microscopic dynamics at the interface [28]. Figure 6(a) shows an example of the simultaneous tracking of the needle and particle motions, enabling analysis of microscopic dynamics under shear. Specifically, we prepare a monolayer of PS particles at the water-decane interface with an area fraction of 30.3%. We then track particle motions using a widely used algorithm [20,29]. The particle monolayer shows a crystalline structure. Although no reliable rheology data can be obtained at such a low area fraction due to the nonlinear shear profile, we observe *sporadic* shearinduced local nonaffine particle rearrangements along grain boundaries, highlighted in the dashed square region of Fig. 6(a) and the dashed line in Fig. 6(b). In order to correlate the monolayer structure with the particle rearrangements, we identify the closest neighbors of particles and calculate the local bond-order parameter  $\psi_6$  as [22],

$$\psi_6 = \frac{1}{N_{\rm r}} \sum_{n=1}^{N_{\rm r}} e^{i6\theta(\vec{r}_n - \vec{r}_0)},\tag{9}$$

where we count all the  $N_r$  neighbors of a particle at  $\vec{r}_0$  within a distance of 2.75 particle diameters and  $\theta(\vec{r}_n - \vec{r}_0)$  is the angle between a fixed axis and the vector from the particle to its neighbor at  $\vec{r}_n$ . The magnitude  $|\psi_6| \in [0, 1]$  characterizes the degree of the local hexagonal order, while the complex phase demonstrates the local lattice director. We identify the presence of grain boundaries by the relative value of  $|\psi_6|$ . As shown in Fig. 6(b), the dots with smaller sizes indicate the defects with  $|\psi_6| < 0.9$ , where particle rearrangements are most likely to happen (the dashed line) [30]. The particle rearrangements are depicted by the displacement vectors in Fig. 6(c).

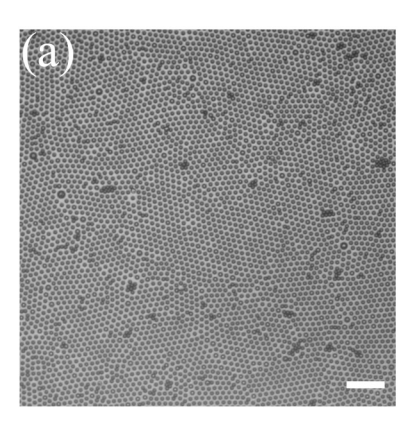
## **IV. CONCLUSION**

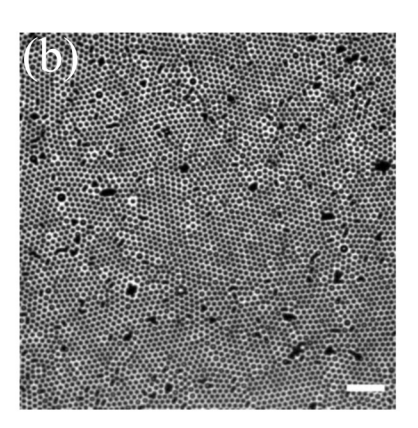
By combining a pair of stationary permanent magnets with a single magnetic coil, we have constructed a compact miniature interfacial stress rheometer (mini-ISR), which is easily adaptable to any commercial microscope. The mini-ISR provides a convenient tool for simultaneous measurements of macroscopic rheology, velocity profiles, and microscopic particle dynamics at a fluid interface. Compared with the existing designs of ISRs, the new design is much simpler, more portable and cost-effective, and can be readily constructed via 3D printing for sensitive interfacial rheology measurements. In particular, the direct coupling between the mini-ISR and a conventional microscope would allow researchers to take advantage of well-developed commercially available microscope systems, which not only improves the imaging quality and reduces operation difficulty but also substantially lowers the construction cost of ISRs. Since optical microscopes are commonly accessible, we believe the new ISR will be broadly used by many experimentalists who have the need to conduct interfacial rheometry. Because of the small surface area associated with the compact design, the mini-ISR may also facilitate the study of the interfacial rheology of expensive or scarce materials such as drug-encapsulated microparticles [31] and custom-made particles like Janus particles [32].

## **APPENDIX: MATERIALS AND METHODS**

## 1. Camera synchronization

A USB-based high-speed analog and digital I/O module (USB-1208HS-2AO, Measurement Computing Corporation) is





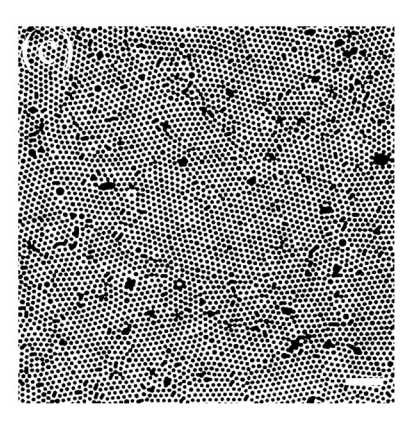


**FIG. 7.** Area fraction determination. (a) A raw image taken with the inverted microscope. (b) The processed image after applying a bandpass filter to remove large-scale illumination variations in (a). (c) The image after applying a binary threshold, which gives an area fraction of 45.6%. The scale bars are  $50 \,\mu\text{m}$ .

used to synchronize imaging with the coil current from the power amplifier. We generate two synchronous analog waveforms in MATLAB. One analog waveform creates a sinusoidal voltage for the input of the signal amplifier, and the other analog waveform uses a square waveform to trigger the camera. For the camera used in our setup (Basler acA2040-90um USB 3.0), a frame is triggered every time the signal goes from 0 to 5 V.

## 2. Preparation of the interface

The interfacial rheological measurements are performed at a water-decane interface. First, 10 mL of de-ionized water is added as the subphase, followed by 10 mL of decane (Sigma-Aldrich) as the superphase. Then, we use tweezers to gently place the magnetized steel needle at the interface. After performing the calibration process at the clean water-decane interface, we measure the rheological behaviors of particle monolayers.

Sulfate-modified polystyrene particles (diameter  $4.10 \pm 0.13 \,\mu\text{m}$ ) are purchased from Thermo Fisher Scientific (lot No. 1876103) as an aqueous dispersion containing 4% w/v particles. The suspension is further diluted by mixing 10% w/v suspension with 45% w/v isopropanol alcohol (VWR International) and 45% w/v distilled de-ionized water (Millipore Direct-Q 3) as the spreading solution. After being sonicated for 30 min, the spreading solution is gently placed at the liquid-liquid interface to form an interfacial monolayer.

We note that it takes time for the particles to reach equilibrium at the interface. We generally wait for 10 min after adding the spreading solution into the rheometer and then apply the largest possible strain for 10 min. After stopping the shearing of the needle and waiting for 10 min, no particle motions are observed. Afterward, the samples are ready for interfacial rheological measurements.

## 3. Area fraction determination

The lowest area fraction (45.6%) is estimated with ImageJ. First, a bandpass filter is applied to the raw image with an upper limit of 150 pixels ( $\sim$ 97.5  $\mu$ m), in order to remove large-scale variations in illumination intensity. Then, we apply a binary threshold and the pixels that represent particles become dark, as shown in Fig. 7.

For the calculation of higher area fractions, we consider a linear relationship between the area fraction and the volume of the spreading solution. We use the lowest area fraction (45.6%, 70  $\mu$ l spreading solution) as the reference. For example, adding the spreading solution of 100  $\mu$ l will result in the area fraction of  $100/70 \times 45.6\% = 65.1\%$ .

### **ACKNOWLEDGMENTS**

The authors acknowledge financial support from the U.S. National Science Foundation (Nos. 1702352 and 2032354). The authors thank the helpful discussions with Joseph Zasadzinski and Xiaolei Ma.

## **REFERENCES**

- Scriven, L., "Dynamics of a fluid interface equation of motion for Newtonian surface fluids," Chem. Eng. Sci. 12, 98–108 (1960).
- [2] Wasan, D., L. Gupta, and M. Vora, "Interfacial shear viscosity at fluidfluid interfaces," AIChE J. 17, 1287–1295 (1971).
- [3] Tajuelo, J., J. Pastor, F. Martínez-Pedrero, M. Vázquez, F. Ortega, R. Rubio, and M. Rubio, "Magnetic microwire probes for the magnetic rod interfacial stress rheometer," Langmuir 31, 1410–1420 (2015).
- [4] Reynaert, S., C. F. Brooks, P. Moldenaers, J. Vermant, and G. G. Fuller, "Analysis of the magnetic rod interfacial stress rheometer," J. Rheol. 52, 261–285 (2008).
- [5] Fuller, G. G., and J. Vermant, "Complex fluid-fluid interfaces: Rheology and structure," Annu. Rev. Chem. Biomol. Eng. 3, 519–543 (2012).
- [6] Mannheimer, R., and R. Schechter, "The theory of interfacial viscoelastic measurement by the viscous-traction method," J. Colloid Interface Sci. 32, 225–241 (1970).
- [7] Goodrich, F., L. H. Allen, and A. Poskanzer, "A new surface viscometer of high sensitivity. I. Theory," J. Colloid Interface Sci. 52, 201–212 (1975).
- [8] Gaub, H., and H. McConnell, "Shear viscosity of monolayers at the air-water interface," J. Phys. Chem. 90, 6830–6832 (1986).
- [9] Choi, S., S. Steltenkamp, J. Zasadzinski, and T. Squires, "Active microrheology and simultaneous visualization of sheared phospholipid monolayers," Nat. Commun. 2, 1–6 (2011).
- [10] Sacchetti, M., H. Yu, and G. Zografi, "Hydrodynamic coupling of monolayers with subphase," J. Chem. Phys. 99, 563–566 (1993).

[11] Tajuelo, J., J. Pastor, and M. A. Rubio, "A magnetic rod interfacial shear rheometer driven by a mobile magnetic trap," J. Rheol. 60, 1095–1113 (2016).

- [12] Shahin, G. T., "The stress deformation interfacial rheometer," Ph.D. thesis (Graduate School of Arts and Sciences, University of Pennsylvania, 1986).
- [13] Brooks, C. F., G. G. Fuller, C. W. Frank, and C. R. Robertson, "An interfacial stress rheometer to study rheological transitions in monolayers at the air-water interface," Langmuir 15, 2450–2459 (1999).
- [14] Naumann, C., C. Brooks, G. Fuller, W. Knoll, and C. Frank, "Viscoelastic properties of lipopolymers at the air-water interface: A combined interfacial stress rheometer and film balance study," Langmuir 15, 7752–7761 (1999).
- [15] Cicuta, P., E. J. Stancik, and G. G. Fuller, "Shearing or compressing a soft glass in 2D: Time-concentration superposition," Phys. Rev. Lett. 90, 236101 (2003).
- [16] Krägel, J., and S. R. Derkatch, "Interfacial shear rheology," Curr. Opin. Colloid Interface Sci. 15, 246–255 (2010).
- [17] Keim, N. C., and P. E. Arratia, "Mechanical and microscopic properties of the reversible plastic regime in a 2D jammed material," Phys. Rev. Lett. 112, 028302 (2014).
- [18] Fitzgibbon, S., E. S. Shaqfeh, G. G. Fuller, and T. W. Walker, "Scaling analysis and mathematical theory of the interfacial stress rheometer," J. Rheol. 58, 999–1038 (2014).
- [19] Verwijlen, T., P. Moldenaers, H. A. Stone, and J. Vermant, "Study of the flow field in the magnetic rod interfacial stress rheometer," Langmuir 27, 9345–9358 (2011).
- [20] Allan, D. B., T. Caswell, N. C. Keim, and C. M. van der Wel, trackpy: Trackpy v0.4.1, 2018.
- [21] Reynaert, S., P. Moldenaers, and J. Vermant, "Interfacial rheology of stable and weakly aggregated two-dimensional suspensions," Phys. Chem. Chem. Phys. 9, 6463–6475 (2007).

- [22] Keim, N. C., philatracks v0.2, zenodo, 2014.
- [23] Barman, S., and G. F. Christopher, "Role of capillarity and microstructure on interfacial viscoelasticity of particle laden interfaces," J. Rheol. 60, 35–45 (2016).
- [24] Rahman, S. E., N. Laal-Dehghani, and G. F. Christopher, "Interfacial viscoelasticity of self-assembled hydrophobic/hydrophilic particles at an air/water interface," Langmuir 35, 13116–13125 (2019).
- [25] Sánchez-Puga, P., J. Tajuelo, J. M. Pastor, and M. A. Rubio, "Flow field-based data analysis in interfacial shear rheometry," Adv. Colloid Interface Sci. 288, 102332 (2020).
- [26] Renggli, D., A. Alicke, R. H. Ewoldt, and J. Vermant, "Operating windows for oscillatory interfacial shear rheology," J. Rheol. 64, 141–160 (2020).
- [27] Liberzon, A., T. Käufer, A. Bauer, P. Vennemann, and E. Zimmer, Openpiv/openpiv-python: Openpiv-python v0.23.4, 2021.
- [28] Mendoza, A. J., E. Guzmán, F. Martínez-Pedrero, H. Ritacco, R. G. Rubio, F. Ortega, V. M. Starov, and R. Miller, "Particle laden fluid interfaces: Dynamics and interfacial rheology," Adv. Colloid Interface Sci. 206, 303–319 (2014).
- [29] Crocker, J. C., and D. G. Grier, "Methods of digital video microscopy for colloidal studies," J. Colloid Interface Sci. 179, 298–310 (1996).
- [30] Keim, N. C., and P. E. Arratia, "Role of disorder in finite-amplitude shear of a 2D jammed material," Soft Matter 11, 1539–1546 (2015).
- [31] Aliaghaie, M., H. Mirzadeh, E. Dashtimoghadam, and S. Taranejoo, "Investigation of gelation mechanism of an injectable hydrogel based on chitosan by rheological measurements for a drug delivery application," Soft Matter 8, 7128–7137 (2012).
- [32] Dietrich, K., G. Volpe, M. N. Sulaiman, D. Renggli, I. Buttinoni, and L. Isa, "Active atoms and interstitials in two-dimensional colloidal crystals," Phys. Rev. Lett. 120, 268004 (2018).